

Draft of February 4, 2008

Massive Protoplanetary Disks in the Trapezium Region

J. A. Eisner¹

University of California at Berkeley

Department of Astronomy

601 Campbell Hall

Berkeley, CA 94720

jae@astron.berkeley.edu

and

John M. Carpenter

California Institute of Technology

Department of Astronomy MC 105-24

Pasadena, CA 91125

jmc@astro.caltech.edu

ABSTRACT

We determine the disk mass distribution around 336 stars in the young (~ 1 Myr) Orion Nebula cluster by imaging a $2.5' \times 2.5'$ region in $\lambda 3$ mm continuum emission with the Owens Valley Millimeter Array. For this sample of 336 stars, we observe 3 mm emission above the 3σ noise level toward ten sources, six of which have also been detected optically in silhouette against the bright nebular background. In addition, we detect 20 objects in 3 mm continuum emission that do not correspond to known near-IR cluster members. Comparisons of our measured fluxes with longer wavelength observations enable rough separation of dust emission from thermal free-free emission, and we find substantial dust emission toward most objects. For the sample of ten objects detected at both 3 mm and near-IR wavelengths, eight exhibit substantial dust emission. Excluding the two high-mass stars ($\theta^1\text{OriA}$ and the BN object) and assuming a gas-to-dust

¹Miller Fellow

ratio of 100, we estimate circumstellar masses ranging from 0.13 to $0.39 M_{\odot}$. For the cluster members not detected at 3 mm, images of individual objects are stacked to constrain the mean 3 mm flux of the ensemble. The average flux is detected at the 3σ confidence level, and implies an average disk mass of $0.005 M_{\odot}$, comparable to the minimum mass solar nebula. The percentage of stars in Orion surrounded by disks more massive than $\sim 0.1 M_{\odot}$ is consistent with the disk mass distribution in Taurus, and we argue that massive disks in Orion do not appear to be truncated through close encounters with high-mass stars. Comparison of the average disk mass and number of massive dusty structures in Orion with similar surveys of the NGC 2024 and IC 348 clusters is used to constrain the evolutionary timescales of massive circumstellar disks in clustered environments.

Subject headings: Galaxy:Open Clusters and Associations:Individual: Orion, Stars:Planetary Systems:Protoplanetary Disks, Stars: Pre-Main-Sequence

1. Introduction

Over the last two decades, high resolution millimeter, infrared, and optical images have provided evidence for the existence of circumstellar disks on scales of ~ 0.1 – 1000 AU around young stars (e.g., Koerner & Sargent 1995; Dutrey et al. 1996; Padgett et al. 1999; O’Dell & Wong 1996; Eisner et al. 2004). Circumstellar disks are the likely birth-sites for planetary systems, and determining their ubiquity, properties, and lifetimes is crucial for constraining the timescales and mechanisms of planet formation. The mass distribution of protoplanetary disks is especially important since disk mass is related to the mass of planets that may potentially form. The minimum-mass protosolar nebula, $\sim 0.01 M_{\odot}$ (Weidenschilling 1977; Hayashi 1981), is an informative benchmark against which to compare disk masses around young stars, and such comparisons can constrain the number of protoplanetary disks with the potential to form planetary systems like our own solar system.

While direct imaging at optical through near-IR wavelengths has provided concrete evidence for a limited number of circumstellar disks (e.g., O’Dell & Wong 1996), and observations of near-IR excess emission have shown statistically that most young stars with ages less than a few million years still possess inner circumstellar disks (e.g., Strom et al. 1989; Haisch et al. 2001), these studies did not constrain the disk mass distribution. To probe the bulk of the disk mass, which resides in cooler, outer disk regions, observations of optically-thin millimeter emission are needed.

Several investigators have carried out comprehensive single-dish mm and sub-mm continuum surveys toward regions of star formation comprising loose aggregates of stars: Taurus (Beckwith et al. 1990; Osterloh & Beckwith 1995; Motte & André 2001; Andrews & Williams 2005), ρ Ophiuchi (André & Montmerle 1994; Nuernberger et al. 1998; Motte et al. 1998), Lupus (Nuernberger et al. 1997), Chamaeleon I (Henning et al. 1993), Serpens (Testi & Sargent 1998), and MBM 12 (Itoh et al. 2003; Hogerheijde et al. 2002). In Taurus, 37% of stars appear to possess disks more massive than $\sim 0.01 M_{\odot}$, and the median disk mass is $5 \times 10^{-3} M_{\odot}$ (Andrews & Williams 2005). The fraction of massive disks and the median disk mass is comparable in ρ Ophiuchi (André & Montmerle 1994).

Expanding millimeter continuum surveys to include rich clusters allows the determination of accurate statistics on the frequency and evolution of massive disks as a function of both stellar mass and age. Also, since most stars in the Galaxy form in rich clusters (Lada et al. 1991, 1993; Carpenter 2000; Lada & Lada 2003), understanding disk formation and evolution in cluster environments is a vital component in our general understanding of how stars and planets form. The main challenge to observing rich clusters at mm-wavelengths is that very high angular resolution is required to resolve individual sources and to distinguish compact disk emission from the more extended emission of the molecular cloud. Single-aperture mm-wavelength telescopes lack sufficient angular resolution, and to date, only three rich clusters have been observed with mm-wavelength interferometers: the Orion Nebula cluster (Mundy et al. 1995; Bally et al. 1998b; Williams et al. 2005), IC 348 (Carpenter 2002), and NGC 2024 (Eisner & Carpenter 2003).

The enhanced sensitivity of the most recent observations of Orion has enabled the detection of several massive ($\gtrsim 0.01 M_{\odot}$) disks (Williams et al. 2005), while upper limits from other surveys range from ~ 0.025 – $0.17 M_{\odot}$ (Mundy et al. 1995; Bally et al. 1998b). Moreover, extending detection limits by considering as ensembles the large numbers ($\gtrsim 100$) of young stars included in the surveys of IC 348 and NGC 2024 allowed estimates of mean disk masses of ~ 0.002 and $0.005 M_{\odot}$, respectively (Carpenter 2000; Eisner & Carpenter 2003). While it appears that an average star aged $\lesssim 1$ Myr still possesses a massive circumstellar disk, more sensitive observations are necessary to detect directly large numbers of massive disks at a range of ages, and thereby constrain the mass distribution and evolutionary timescales.

Here, we present a new mm-wavelength interferometric survey of the Orion Nebula cluster (ONC), a young, deeply embedded stellar cluster that includes the bright, massive Trapezium stars. The Trapezium region contains hundreds of stars within several arcminutes, and pre-main-sequence evolutionary models (e.g., D'Antona & Mazzitelli 1994) fitted to spectroscopic and/or photometric data indicate that most stars are less than approximately one million years old (e.g., Prosser et al. 1994; Hillenbrand 1997). Moreover, the standard

deviation in the distribution of inferred stellar ages is $\lesssim 1$ Myr (Hillenbrand 1997). Our observations thus provide a snapshot of millimeter emission around a large number of roughly coeval young stars.

With the large number of stars in the ONC, we can begin to investigate the correlation of disk properties with stellar and/or environmental properties. Previous investigations of near-IR excess emission have explored the dependence of inner disk properties on stellar mass, age, and environment (e.g., Hillenbrand et al. 1998; Lada et al. 2000). For example, the fraction of stars in Orion exhibiting near-IR excess emission seems largely independent of stellar age and mass, although there are indications of a paucity of disks around very massive stars (Hillenbrand et al. 1998; Lada et al. 2000). In addition, the inner disk fraction may decrease at larger cluster radii (Hillenbrand et al. 1998). To explore how the properties of the outer disk component correlate with such stellar and environmental properties, millimeter observations of cool, optically-thin dust emission are necessary.

Our observations represent an improvement over previous work because our mosaicked image encompasses more than three times as many sources as the previous surveys, enabling an improvement of $\sqrt{3}$ in estimates of frequency and mean mass of circumstellar disks. Moreover, the comparable sensitivity of this survey with previous observations of IC 348 and NGC 2024 allows a more direct comparison between relatively young (NGC 2024: 0.3 Myr; Meyer 1996; Ali 1996), intermediate (ONC: 1 Myr; Hillenbrand 1997), and old (IC 348: 2 Myr; Luhman et al. 1998; Luhman 1999) clusters, providing constraints on timescales for disk evolution.

2. Observations and Data Reduction

We mosaicked a $2'5 \times 2'5$ region toward the ONC in $\lambda 3$ mm continuum with the OVRO millimeter array between August, 2003 and March, 2004. Continuum data were recorded using the new COBRA correlator, providing a total of 8 GHz of bandwidth centered at 100 GHz. Two different configurations of the 6-element array provided baselines between 35 and 240 meters. As shown in Figure 1, the mosaic consists of sixteen pointing centers. For observations in a given night, the mosaic was observed in its entirety once or twice (depending on the length of the track), with equal integration time (and hence equal sensitivity) for each pointing position.

We calibrated the amplitudes and phases of the data with the blazar J0530+135: $(\alpha, \delta)_{J2000} = (5^{\text{h}}30^{\text{m}}56^{\text{s}}.4, +13^{\circ}31'55''2)$. Three minute observations of J0530+135 were interleaved with sixteen minute integrations on the target mosaic. We estimated the flux for

J0530+135 using Neptune and Uranus as flux calibrators. Since we obtained data over an eight month time-span, and J0530+135 is variable, we estimated the flux for each array configuration. For observations in the less extended “E” configuration (spanning August–September 2003), we calculated a mean flux of 2.91 Jy based on four measurements, and the RMS in the flux measurements was 0.21 Jy. For observations in the “H” configuration (spanning December, 2003–March, 2004), we determined a flux of 2.08 Jy and an RMS of 0.14 Jy using eight measurements. All data calibration was performed using a suite of IDL routines developed for the MIR software package.

We mosaicked the sixteen individual pointings into a single image, robustly weighted the data (using a robust parameter of 0.5), then de-convolved and CLEANed the mosaic using the MIRIAD package (Sault et al. 1995). Since we are primarily interested in compact disk emission, we eliminated uv spacings shorter than $35 k\lambda$ in order to avoid contamination from bright extended emission. The eliminated spacings correspond to size scales larger than $\sim 6''$. The cutoff value was chosen to minimize the RMS background noise in the CLEANed image. We note that previous analyses of the ONC have also eliminated data with uv spacings $< 35 k\lambda$ (Felli et al. 1993a; Bally et al. 1998b) to filter out the extended emission in the region.

The mosaic produced from our robust-weighted data with $r_{uv} > 35 k\lambda$ is shown in Figure 2. The unit gain region of the mosaic encompasses a $2'5 \times 2'5$ area, as indicated by the solid curve. The FWHM of the synthesized beam is $1''.9 \times 1''.5$. The RMS varies across the mosaic, because of varying amounts of sidelobe emission from point sources and extended emission that were not removed by CLEAN. We calculate the RMS of the image in $0'5 \times 0'5$ sub-regions, and find values ranging from 0.88 mJy to 2.34 mJy. Despite these variations in RMS, the noise across the mosaic is largely Gaussian and the “effective” noise for the mosaic is 1.75 mJy (Figure 3).

3. Results and Analysis

3.1. Detected Sources

When searching for detections, we begin by considering only the positions of known near-IR cluster members (Hillenbrand & Carpenter 2000) that lie within the unit gain contour of our OVRO mosaic (Figure 2). For these 336 pre-determined positions, ~ 0.4 sources are expected to show emission above the 3σ level from Gaussian noise, and we therefore employ a 3σ detection threshold, where σ is the noise determined locally in $0'5 \times 0'5$ sub-regions.

In order to determine whether 3 mm continuum emission is coincident with near-IR

source positions, we estimate relative positional uncertainties from the centroiding uncertainty for millimeter sources ($\sim 0.5\theta_{\text{beam}}/\text{signal-to-noise} \approx 0.^{\circ}3$) and the uncertainty in the near-IR source positions ($\sim 0.^{\circ}3$). The 1σ relative astrometric uncertainty is $\sim 0.^{\circ}4$, and only objects for which the millimeter emission lies within $0.^{\circ}4$ of the K -band stellar position are claimed as coincident. We detect 3 mm continuum emission above the 3σ level toward 10 near-IR detected objects (Table 1). The 3 mm emission for these detections appears point-like, with FWHM comparable to that of the synthesized beam. OVRO 3mm continuum images of detected sources coincident with near-IR cluster member positions are displayed in Figure 4.

One of the sources detected at both near-IR and 3 mm wavelengths is the BN object (Becklin & Neugebauer 1967), and six others correspond with optically- and radio-detected proplyds (O'Dell et al. 1993; Felli et al. 1993a,b). Although Gaussian noise is expected to produce less than one false detection, there may still be chance coincidences with sidelobe artifacts in regions containing bright, nearby 3 mm emission sources. Thus, HC 178 and HC 192, which occur in crowded areas displaying bright positive and negative emission (Figure 4), should be regarded with some caution.

We also search for detections in the mosaic toward positions that do not correspond with known ONC cluster members. For the entire mosaic, which contains substantially more pixels than those considered for near-IR detected objects, a 5σ detection limit is employed to ensure that we are not “detecting” noise spikes in the image: less than one pixel in the entire image should exhibit a noise spike greater than 5σ . Twenty additional objects, without near-IR counterparts, are detected in 3 mm continuum emission above the 5σ level (Table 1). Since many of these detections occur in crowded regions (Figure 2), listed fluxes for these objects may be contaminated by sidelobe emission from other nearby sources.

3.2. Dust and Free-Free Emission

Free-free emission arises in hot ionized gas, and in the ONC such conditions may exist either in HII regions around high-mass stars (e.g., Garay et al. 1987) or in the outer regions of disks or envelopes that are irradiated by the hot Trapezium stars (e.g., O'Dell et al. 1993). Our 3 mm fluxes may thus trace some free-free emission from hot gas in addition to thermal continuum emission from cool dust. Because the spectral shape of free-free radiation differs from that of thermal dust emission, comparing our 3 mm measurements with longer-wavelength data enables us to distinguish these components. Moreover, radio wavelength observations have sufficient sensitivity ($\lesssim 0.3$ mJy; Felli et al. 1993b) to detect all of the sources detected in our 3 mm mosaic, if the 3 mm flux traces free-free emission.

We model our observed 3 mm continuum fluxes including both free-free and dust emission. The free-free emission is parameterized by a turnover frequency, ν_{turn} , which demarcates where the radiation switches from optically-thick to optically-thin, and by the flux at this frequency, $F_{\nu,\text{turn}}$:

$$F_{\nu,\text{ff}} = \begin{cases} F_{\nu,\text{turn}}(\nu/\nu_{\text{turn}})^{-0.1} & \text{if } \nu \geq \nu_{\text{turn}} \\ F_{\nu,\text{turn}}(\nu/\nu_{\text{turn}})^2 & \text{if } \nu \leq \nu_{\text{turn}} \end{cases}. \quad (1)$$

Emission from cool dust is added to this free-free emission to obtain a model of the observed flux. We assume that

$$F_{\nu,\text{dust}} = F_{3\text{mm},\text{dust}}(\nu/100 \text{ GHz})^{(2+\beta)} = F_{3\text{mm},\text{dust}}(\nu/100 \text{ GHz})^3, \quad (2)$$

for $\beta = 1$ (e.g., Beckwith et al. 1990).

We estimate the relative contributions of dust and free-free emission by fitting this model, $F_{\nu} = F_{\nu,\text{ff}} + F_{\nu,\text{dust}}$, to our measured 3 mm fluxes and 3.5 mm, 2 cm, 6 cm, and 20 cm fluxes from the literature (Mundy et al. 1995; Felli et al. 1993a,b). Given the noise level of the centimeter observations ($\lesssim 0.3$ mJy; Felli et al. 1993a,b) and our measured 3 mm fluxes ($\gtrsim 10$ mJy), for objects undetected at centimeter wavelengths, less than 3% of the 3 mm emission can be free-free. For simplicity, we attribute 100% of the 3 mm flux to dust emission for these objects. For objects detected at centimeter wavelengths, we fit the dust+free-free model to the ≥ 4 flux measurements for each source, and thus we are able to determine the three free parameters of the model, ν_{turn} , $F_{\nu,\text{turn}}$, and $F_{3\text{mm},\text{dust}}$. Long-wavelength fluxes and models are plotted in Figure 5, and the fluxes due to thermal dust emission are listed in column 5 of Table 1. Uncertainties for these dust fluxes are given by the 1σ uncertainties of the model fits.

Three of the objects in Table 1 that are also seen at near-IR wavelengths (HC 178, HC 192, and HC 282) were undetected at longer wavelengths, indicating that the 3 mm emission probably traces dust. Moreover, although HC 774 is detected at 20 cm, it is undetected at either 2 or 6 cm, indicating that the long-wavelength measurement probably traces some non-thermal, variable emission mechanism, while the OVRO flux likely arises from cool dust emission. For the remaining 6 sources, which were also detected in the 2-20 cm surveys of Felli et al. (1993a,b), at least some components of the measured 3 mm fluxes are likely due to free-free emission. While for most objects some of the observed flux probably arises from dust emission, for HC 322 and HC 323, 100% of the 3 mm flux may be due to free-free emission. Observations at $850 \mu\text{m}$ showed that even at shorter wavelengths, 100% of the emission from HC 323 may be free-free, while HC 322 probably has some emission from cool dust (Williams et al. 2005).

Because HC 336 ($\theta^1\text{OriA}$) is highly variable at centimeter wavelengths (Felli et al. 1993b), the flux due to dust listed in Table 1 is uncertain. Previous observations at 3.5

mm wavelength did not detect this object above an RMS noise level of ~ 2 mJy (Mundy et al. 1995); our measured flux of ~ 20 mJy indicates that this object is also highly variable at millimeter wavelengths, arguing for non-thermal emission. Thus, the flux component attributed to dust in Table 1 is an upper limit.

Among the sources detected at 3 mm but not at near-IR wavelengths, only one is detected at wavelengths ≥ 2 cm, IRc2. For this object, only $\sim 1\%$ of the flux can be attributed to free-free emission. Two other objects (MM8 and MM14) are detected at 1.3 cm wavelength with flux densities $\lesssim 1$ mJy (Zapata et al. 2004); the measured 3 mm flux densities are $\gtrsim 20$ times higher (Table 1). Thus, it appears that free-free emission does not contribute substantially to the 3 mm flux from objects without near-IR counterparts; the lack of free-free emission may indicate that these sources are very embedded in the cloud, shielded from ionizing radiation.

In our calculation of the relative contributions to the 3 mm flux of free-free and dust emission, we assumed that $\beta = 1$. In fact, β may be smaller if grains are substantially larger in protoplanetary disks than in the interstellar medium (e.g., Miyake & Nakagawa 1993; Andrews & Williams 2005). However, the assumed value of β is not crucial to our calculations. If we instead assume that $\beta = 0$, the derived component of the 3 mm flux due to dust changes by only a few percent or less.

3.3. Circumstellar Masses

The mass of circumstellar material (dust + gas, assuming a standard ISM gas to dust mass ratio of 100) is related to the component of the 3 mm continuum flux due to dust emission. Assuming the emission is optically-thin, and following Hildebrand (1983),

$$M_{\text{circumstellar}} = \frac{S_{\nu, \text{dust}} d^2}{\kappa_\nu B_\nu(T_{\text{dust}})}. \quad (3)$$

Here, ν is the observed frequency, $S_{\nu, \text{dust}}$ is the observed flux due to cool dust, d is the distance to the source, $\kappa_\nu = \kappa_0 (\nu/\nu_0)^\beta$ is the mass opacity, T_{dust} is the dust temperature, and B_ν is the Planck function. We assume $d = 480$ pc (Genzel et al. 1981), $\kappa_0 = 0.02 \text{ cm}^2 \text{ g}^{-1}$ at $1300 \mu\text{m}$, $\beta = 1.0$ (Hildebrand 1983; Beckwith et al. 1990), and $T_{\text{dust}} = 20 \text{ K}$ (based on the average dust temperature inferred for Taurus; Andrews & Williams 2005; see also the discussion in Carpenter 2002; Williams et al. 2005). While it is possible that external heating by the massive Trapezium stars will lead to higher disk temperatures than in Taurus, we nevertheless assume that $T_{\text{dust}} = 20 \text{ K}$ for consistency with previous studies. Uncertainties in the assumed values of T_{dust} and κ imply that the derived masses are uncertain (in an

absolute sense) by at least a factor of 3 (e.g., Pollack et al. 1994). With our assumed values for these parameters, the masses of detected sources in our OVRO mosaic (Table 1) range from 0.13 to $1.45 M_{\odot}$.

Since some of the objects in Table 1 may be massive stars, the millimeter flux may contain contributions from dust substantially hotter than the assumed 20 K. The high luminosity of the BN object ($\sim 2500 L_{\odot}$) implies a spectral type of B3-B4 (Gezari et al. 1998), and the luminosity of $\theta^1\text{OriA}$ implies a spectral type of O7 (Warren & Hesser 1977). In addition, IRc2 is probably a massive star, and the high luminosity of nearby “source I” provides additional dust heating (Gezari et al. 1998). For these sources, the computed dust masses are over-estimated, since smaller masses of hotter dust can produce the observed 3 mm emission (for example, if $T_{\text{dust}} = 50$ K then the computed dust masses would be lower by a factor of 3.3). The circumstellar masses listed in Table 1 for BN (HC 705), $\theta^1\text{OriA}$ (HC 336), and IRc2 (MM 3) should therefore be treated as upper limits. Other detected objects do not have known stellar masses, but are likely to be low-mass stars (see §3.5). Thus, the assumptions in Equation 3 are plausible for most of the objects in Table 1.

3.4. Circumstellar Geometry

Our OVRO observations alone do not have the angular resolution or kinematic information necessary to determine whether the circumstellar material is distributed in disks or envelopes, or combinations of the two. Where 3 mm emission is detected toward known near-IR cluster members, the fact that the near-IR light is visible despite the high extinctions ($A_V \gtrsim 300$) that would arise for dust masses inferred from the 3 mm fluxes (for spherically distributed material) implies that the dust lies in flattened, disk-like distributions (see also, e.g., Beckwith et al. 1990; Eisner & Carpenter 2003). There are, however, exceptions to this argument.

Massive stars may be surrounded by hotter dust than low-mass stars, and for these objects smaller dust masses (with smaller associated extinction of near-IR light) can produce the observed emission. Furthermore, the high extinctions ($A_V \sim 20 - 60$ mags; Gezari et al. 1998) observed toward the high-mass stars detected at 3 mm could be consistent with spherically distributed material. Thus, we cannot necessarily infer a flattened distribution of dust around $\theta^1\text{OriA}$ or BN based on the observed 3 mm fluxes. However, most of the stars in our observations have masses $\lesssim 1 M_{\odot}$ (e.g., Hillenbrand & Carpenter 2000), and thus the extinction argument generally applies, suggesting that most objects detected in both millimeter and near-IR emission trace flattened structures.

Our claim that objects detected in both 3 mm and near-IR emission are flattened structures is bolstered by the fact that six of the detected sources correspond to proplyds observed by O’Dell et al. (1993), and some of these show flattened disk-like morphologies (Bally et al. 1998a). This is particularly striking for HC 774, where optical images show a flattened ring-like structure surrounding a central, extincted star (Bally et al. 1998a). However, we can not be sure that flattened structures observed around these stars are geometrically thin disks in Keplerian rotation, as opposed to flattened disk+envelope structures such as those inferred around some Class I objects (e.g., Eisner et al. 2005).

3.5. Ensemble of Non-Detected Sources

Only 3% of the known near-IR cluster members in the Trapezium region are detected in 3 mm continuum emission, and thus the vast majority of objects are undetected in our observations. In order to examine the flux distribution for “typical” low-mass stars in the ONC, we consider the distribution of 3 mm fluxes observed for the ensemble of the remaining 326 undetected near-IR cluster members; the large number of sources allows an enhanced sensitivity for the ensemble compared to that for an individual object.

While spectra are unavailable for most of the stars in the central region of the cluster (where we are observing), for the ~ 125 objects within the unit gain contour where spectra have been obtained, $\sim 85\%$ have stellar masses $\leq 1 M_{\odot}$ (Hillenbrand 1997; Luhman et al. 2000). Furthermore, near-infrared photometric studies of all sources within the unit gain contour confirm that most stars have masses between 0.1 and $1 M_{\odot}$ (Hillenbrand & Carpenter 2000).

Figure 6 shows the distribution of mm-wavelength fluxes observed toward 326 K -band sources in the ONC, none of which are detected individually above the 3σ level. The 30 bright point sources visible in Figure 2 were removed using CLEAN before computing this histogram. We also plot the flux distribution measured for all other pixels within the unit gain contour (after subtraction of bright point sources). The mean flux observed for the ensemble of 326 near-IR cluster members is 0.267 mJy, and the standard deviation of the mean is 8.75×10^{-5} Jy. The flux distribution is thus biased to positive values with respect to the noise distribution, and the significance of this bias is 3σ . It appears that while none of these K -band objects are detected individually in 3 mm continuum emission above the 3σ level, there may be weak emission below the 3σ level from circumstellar disks.

This positive bias is also illustrated in the right panel of Figure 6, which shows an average image of the 3 mm flux observed toward K -band sources, obtained by averaging $10'' \times 10''$

images centered around each object. We CLEANed this average image in order to remove negative features associated with sidelobe emission. However, some negative features remain, presumably as a result of residual calibration errors which prevent perfect CLEANing.

The “average” disk is detected at a significance of $\sim 3\sigma$, and is centered on the mean position of K -band sources (within positional uncertainties). In addition, the FWHM of the emission in Figure 6, $2.^{\circ}5 \times 1.^{\circ}3$, is comparable to the FWHM of the beam, suggesting that the positive bias observed in Figure 6 represents underlying weak mm-wavelength emission from point sources. We conclude that the average flux is dominated by small-scale emission such as that expected for circumstellar disks.

Because the sensitivity of previous radio-wavelength surveys (Felli et al. 1993a,b) is comparable to this average flux, we can not rule out some contribution of free-free emission to the mean flux. While the average flux arising from cool dust emission may therefore be somewhat lower than 0.27 mJy, we ignore this effect here, and await more sensitive long-wavelength observations to provide better constraints on low levels of free-free emission. For the 326 known K -band sources, which predominantly have stellar masses between 0.1 and 1 M_{\odot} (Hillenbrand & Carpenter 2000), our assumptions in Equation 3 should be valid, and the conversion from 3 mm flux into mass should be reliable (modulo the uncertainties concerning free-free emission discussed above). The mean circumstellar mass among the 326 low-mass K -band sources within the unit gain contour of our OVRO mosaic is $0.0055 \pm 0.0018 M_{\odot}$.

4. Discussion

4.1. Frequency of Massive Disks

We detected 30 objects in the ONC in 3 mm continuum emission, 10 of which correspond to near-IR cluster members. As discussed above, for objects detected only in 3 mm emission, we can not determine whether the dust is distributed in disks, envelopes, or combinations of the two. Furthermore, for massive stars the geometry and total mass of circumstellar material are uncertain since the dust may be substantially hotter than we assume above. Thus, we exclude the BN Object and θ^1 OriA from the list of near-IR+mm detected objects when discussing massive disks.

Since our 3σ detection threshold for 3 mm emission corresponds to a mass of $\sim 0.1 M_{\odot}$ (if 100% of the observed flux arises from dust emission), in this section we will consider the statistics of disks more massive than $0.1 M_{\odot}$. For the eight presumably low-mass mm+IR detected sources, the 3 mm emission from two objects (HC 322 and HC 323) is dominated by free-free emission, leaving only six massive disk candidates. Furthermore, the 1σ uncertainty

on the free-free emission contribution to the 3 mm flux for HC 241 cannot exclude a disk mass $\lesssim 0.1 M_{\odot}$. Thus, it appears that at most 6/336 ONC cluster members ($\leq 2\%$) possess massive circumstellar disks.

The large dust mass inferred for some of these objects is higher than typically found for circumstellar disks (e.g., Beckwith et al. 1990). This may imply that some of these young stars are surrounded by flattened disk+envelope structures, such as those inferred around some Class I objects (Eisner et al. 2005). However, we note that the two highest-mass disks are found in crowded regions, and thus the large inferred masses may be contaminated by sidelobe emission from nearby bright sources (Figure 4; §3.1).

Our observations did not find large millimeter fluxes toward the positions of most near-IR cluster members in the ONC: $\leq 2\%$ of the near-IR cluster members have disk masses higher than $\sim 0.1 M_{\odot}$. Although K-L color excesses of ONC members suggest that $80 \pm 7\%$ of the stars have circumstellar disks (Lada et al. 2000), these two estimates of the disk fraction are not contradictory, since the near-IR emission probes trace material ($\sim 10^{-6} M_{\odot}$) within ~ 0.1 AU of the star, while the millimeter emission traces massive ($\gtrsim 0.1 M_{\odot}$) outer circumstellar material. Furthermore, when treated as an ensemble, millimeter emission is detected from near-IR objects in the mean, implying an average disk mass of $\sim 0.005 M_{\odot}$.

Based on our analysis of the ensemble of non-detected sources, it appears that most stars in the ONC likely possess disks with masses on the order of $0.005 M_{\odot}$. Thus, the “average disk” in this region is comparable to the minimum mass solar nebula ($\sim 0.01 M_{\odot}$; Weidenschilling 1977), indicating that most stars in the Trapezium region may be capable of forming solar systems like our own. Since most stars in the Galaxy, including our sun, probably formed in regions like Orion, it seems that the capability to form analogs of our solar system is fairly common.

Our survey covered a larger field than the recent observations of Williams et al. (2005), but with a lower mass sensitivity. Because Williams et al. (2005) observed at 850 μ m, even though their flux sensitivity (2.7 mJy) was poorer than ours (~ 1.75 mJy), the steep spectral dependence of dust emission (Equation 2) means that their observations were sensitive to smaller dust masses. Thus, Williams et al. (2005) detected three additional objects (OW 170-337, OW 171-334, and OW 171-340) with circumstellar masses of $\sim 0.01 M_{\odot}$, which were below our detection threshold. However, the larger area covered by our mosaic allowed us to detect emission from massive disks around four proplyds (OW 177-341, OW 158-327, OW 158-314, and OW 182-413) that were outside of the Williams et al. (2005) survey area.

4.2. Dependence of Disk Properties on Environment

It has been suggested that circumstellar disks in clustered environments may be truncated due to close encounters with massive stars resulting in either tidal stripping or photo-evaporation of outer disk material (e.g., Scally & Clarke 2001). Evidence of this hypothesis has recently been inferred from the observation that brown dwarfs appear more common in the ONC than in the lower-stellar-density Taurus region (e.g., Kroupa & Bouvier 2003), although this result and its interpretation remain controversial (e.g., Guieu et al. 2005). While the observations presented here do not have sufficient angular resolution to spatially resolve the outer disk radius, we can test the truncation hypothesis by comparing the disk mass distribution in the ONC and Taurus since truncated disks will be less massive than un-truncated disks.

As discussed in §4.1, we detected disks more massive than $\sim 0.1 M_{\odot}$ around $\leq 2\%$ of low-mass ONC cluster members. For comparison, $\sim 1.2\%$ of Taurus stars possess such massive disks (Beckwith et al. 1990; Osterloh & Beckwith 1995; Andrews & Williams 2005). The average disk masses in the two regions are also comparable. Thus, the fraction of massive disks in Taurus and Orion appears similar, arguing against the hypothesis that massive disks are truncated through close encounters with high-mass cluster members. We caution, however, that if dust temperatures in the ONC are systematically higher than in Taurus (Equation 3; §3.3), then the percentage of high-mass disks in the ONC would be reduced relative to Taurus.

Environmental effects on massive disks can also be investigated through the dependence of disk properties on cluster radius. We therefore consider the positions of the six massive disks detected in our observations (i.e., the subset of the 10 near-IR+mm detected objects that are not massive stars and are not dominated by free-free emission; see §4.1) relative to the cluster center, which we define to lie roughly in the middle of the four bright Trapezium stars at $(\alpha, \delta)_{J2000} = (5^{\text{h}}35^{\text{m}}16.34^{\text{s}}, -5^{\circ}23'15''6)$. Within $10''$ of the cluster center, 8% of stars (1/13) possess massive disks, while this percentage falls to 4% (1/25) between $10''$ and $20''$, and never higher than 5% in successive annuli throughout the remainder of the unit gain contour (4/290 sources with radii $\geq 20''$). While projection effects may complicate the interpretation of this apparent trend, the marginally higher percentage of massive disks close to the massive Trapezium stars provides some further support against the hypothesis of disk truncation through close encounters.

Although the distribution of massive disks in the ONC can not be distinguished from that of Taurus, previous observations of the disk mass distributions in the rich clusters NGC 2024 (Eisner & Carpenter 2003) and IC 348 (Carpenter 2002) showed a statistically significant difference from Taurus. Based on these earlier results, we argued previously

that the physical conditions in rich clusters might be responsible for observed differences between clustered and isolated environments. More sensitive interferometric observations are necessary to detect millimeter emission from a larger sample of disks, to place more definitive constraints on correlations of disk mass with environment.

4.3. Disk Evolution

We compare our results for the ONC with analogous 3 mm continuum surveys of NGC 2024 (Eisner & Carpenter 2003) and IC 348 (Carpenter 2002). NGC 2024 and IC 348, are somewhat less dense than the ONC, but still each contain on the order of 300 stars (Lada et al. 1991; Herbig 1998). In addition, spectroscopically-determined masses in the ONC (Hillenbrand 1997) and IC 348 (Luhman 1999), and estimated masses from color-magnitude diagrams in NGC 2024 (Meyer 1996; Eisner & Carpenter 2003) indicate similar stellar mass ranges in the three clusters, although the spectral types of the most massive stars are somewhat cooler in NGC 2024 (\sim O8; Bik et al. 2003) and IC 348 (B5; Luhman et al. 1998) than in Orion. Comparison of the disk mass distributions can provide insights into disk evolution, since the three clusters have apparently different ages. Ages computed by comparing cluster member positions in an HR diagram to the predictions of pre-main-sequence evolutionary tracks (using the same models for each cluster; D’Antona & Mazzitelli 1997), as well as the degree of embeddedness for each cluster indicate that NGC 2024 is probably younger than the ONC, which is in turn younger than IC 348 (Meyer 1996; Ali 1996; Hillenbrand 1997; Luhman et al. 1998; Luhman 1999).

The average disk masses for “typical” stars in the three regions (i.e., the vast majority of cluster members not detected individually in 3 mm emission) is plotted as a function of cluster age in Figure 7. In NGC 2024, the mean disk mass is $0.005 \pm 0.001 M_{\odot}$ (Eisner & Carpenter 2003), compared to 0.0055 ± 0.0018 in the ONC, and $0.002 \pm 0.001 M_{\odot}$ in IC 348 (Carpenter 2002). In addition, the fraction of objects detected in millimeter emission (without near-IR counterparts) is higher in NGC 2024 ($\sim 6\%$) and the ONC ($\lesssim 10\%$) than in IC 348 (0%). In fact, since the observations of the ONC had a poorer 3σ mass sensitivity for individual sources, $0.1 M_{\odot}$ versus $0.035 M_{\odot}$ in NGC 2024 (Eisner & Carpenter 2003) and $0.025 M_{\odot}$ in IC 348 (Carpenter 2002), the fraction of structures in the ONC with comparable masses to those detected in NGC 2024 may be somewhat higher. Assuming that the differences between NGC 2024, the ONC, and IC 348 are due to temporal evolution, these observations indicate that massive disks/envelopes may dissipate on timescales $\lesssim 2$ Myr, and that the average disk mass may decrease by a factor of 2.5 ± 1.3 between ~ 0.3 and 2 Myr.

It is important to keep in mind that the total millimeter emission is sensitive to dust grain properties in addition to total dust mass. For example, a given mass of dust grains larger than the observing wavelength emits less radiation than the same mass of small dust particles, and the millimeter flux therefore depends on dust grain properties in addition to the total mass. Furthermore, the presence of hotter stars in the ONC (relative to NGC 2024 and IC 348) may potentially lead to systematically higher disk temperatures, which would lead to smaller inferred masses (Equation 3): if $T_{\text{dust}} = 50$ K, disk masses would be reduced by a factor of 3.3. Thus, observed evolution in the millimeter flux may indicate that one or more of the assumed quantities in Equation 3 (e.g., temperature or opacity) is different in the three regions.

Regardless of the underlying factors, our measurements provide a 2σ suggestion of evolution between ~ 0.3 and 2 Myr. Future, more sensitive measurements of the disk mass distributions in larger numbers of clusters will decrease the uncertainties in Figure 7, enabling more concrete constraints on the evolutionary timescales of massive disks. Moreover, follow-up observations at multiple wavelengths will begin to break degeneracies between dust grain properties and temperatures, and total disk masses.

5. Conclusions

We observed a $2.5' \times 2.5'$ region of the Orion Nebula cluster in $\lambda 3$ mm continuum emission with the Owens Valley Millimeter Array. The mosaic encompassed 336 young stars in the vicinity of the massive Trapezium stars, and constrained the disk mass distribution for this large number of cluster members.

We detected 30 objects in 3 mm continuum emission above the 3σ limit, 10 of which correspond with near-IR cluster members. Six of these, in turn, also correspond with optically-detected proplyds. Comparison of our measured fluxes with longer wavelength observations enabled rough separation of emission due to dust and that due to thermal free-free emission, and we found that the 3 mm emission toward 8 objects likely arises, in part, from dust.

We argued that with the exception of the massive stars $\theta^1\text{OriA}$ and the BN object, sources detected in both 3 mm and near-IR emission are probably young stars surrounded by disks, and we computed circumstellar masses of $0.13\text{--}0.39 M_\odot$ based on observed 3 mm fluxes (these masses are uncertain by at least a factor of three due to uncertainties in converting flux into mass). Since the vast majority ($\gtrsim 98\%$) of near-IR cluster members do not possess disks more massive than $\sim 0.1 M_\odot$, we placed constraints on lower-mass disks by considering the ensemble of 326 non-detected, predominantly low-mass stars. For the ensemble, we computed

an average disk mass of $0.005 M_{\odot}$, which has a statistical significance of 3σ (although the absolute value of the mass contains larger uncertainties related to converting flux into mass).

The average disk in the ONC is thus comparable to the minimum mass solar nebula, suggesting that most young ($\lesssim 1$ Myr) stars in richly clustered environments (and by extension, most stars in the Galaxy) are surrounded by sufficient circumstellar masses to form solar systems like our own. Furthermore, we found that the frequency of massive disks in the ONC appears similar to that in Taurus, perhaps refuting suggestions that disks in Orion are truncated due to close encounters with the massive Trapezium stars. Finally, we compared the disk mass distributions in three clusters of different ages to begin to constrain the evolutionary timescales of massive disks. Although substantial uncertainties remain, it appears that massive disks may evolve significantly on 1-2 Myr timescales.

Acknowledgments. JAE is currently supported by a Miller Research Fellowship, and acknowledges past support from a Michelson Graduate Research Fellowship. JMC acknowledges support from the Owens Valley Radio Observatory, which is supported by the National Science Foundation through grant AST-9981546. The authors also wish to thank John Bally for providing HST images of the Orion proplyds.

REFERENCES

- Ali, B. 1996, PhD thesis, The Ohio State University, Ohio, USA
- André, P. & Montmerle, T. 1994, ApJ, 420, 837
- Andrews, S. M. & Williams, J. P. 2005, ApJ, 631, 1134
- Bally, J., Sutherland, R. S., Devine, D., & Johnstone, D. 1998a, AJ, 116, 293
- Bally, J., Testi, L., Sargent, A., & Carlstrom, J. 1998b, AJ, 116, 854
- Becklin, E. E. & Neugebauer, G. 1967, ApJ, 147, 799
- Beckwith, S. V. W., Sargent, A. I., Chini, R. S., & Guesten, R. 1990, AJ, 99, 924
- Bik, A., Lenorzer, A., Kaper, L., Comerón, F., Waters, L. B. F. M., de Koter, A., & Hanson, M. M. 2003, A&A, 404, 249
- Carpenter, J. M. 2000, AJ, 120, 3139
- . 2002, AJ, 124, 1593

- D'Antona, F. & Mazzitelli, I. 1994, ApJS, 90, 467
- D'Antona, F. & Mazzitelli, I. 1997, Memorie della Societa Astronomica Italiana, 68, 807
- Dutrey, A., Guilloteau, S., Duvert, G., Prato, L., Simon, M., Schuster, K., & Menard, F. 1996, A&A, 309, 493
- Eisner, J. A. & Carpenter, J. M. 2003, ApJ, 598, 1341
- Eisner, J. A., Hillenbrand, L. A., Carpenter, J. M., & Wolf, S. 2005, ApJ, 635, 396
- Eisner, J. A., Lane, B. F., Hillenbrand, L., Akeson, R., & Sargent, A. 2004, ApJ, 613, 1049
- Felli, M., Churchwell, E., Wilson, T. L., & Taylor, G. B. 1993a, A&AS, 98, 137
- Felli, M., Taylor, G. B., Catarzi, M., Churchwell, E., & Kurtz, S. 1993b, A&AS, 101, 127
- Garay, G., Moran, J. M., & Reid, M. J. 1987, ApJ, 314, 535
- Genzel, R., Reid, M. J., Moran, J. M., & Downes, D. 1981, ApJ, 244, 884
- Gezari, D. Y., Backman, D. E., & Werner, M. W. 1998, ApJ, 509, 283
- Guieu, S., Dougados, C., Monin, J. L., Magnier, E., & Martin, E. L. 2005, A&A, in press
- Haisch, K. E., Lada, E. A., & Lada, C. J. 2001, AJ, 121, 2065
- Hayashi, C. 1981, Progress of Theoretical Physics, 70, 35
- Henning, T., Pfau, W., Zinnecker, H., & Prusti, T. 1993, A&A, 276, 129
- Herbig, G. H. 1998, ApJ, 497, 736
- Hildebrand, R. H. 1983, QJRAS, 24, 267
- Hillenbrand, L. A. 1997, AJ, 113, 1733
- Hillenbrand, L. A. & Carpenter, J. M. 2000, ApJ, 540, 236
- Hillenbrand, L. A., Strom, S. E., Calvet, N., Merrill, K. M., Gatley, I., Makidon, R. B., Meyer, M. R., & Skrutskie, M. F. 1998, AJ, 116, 1816
- Hogerheijde, M. R., Jayawardhana, R., Johnstone, D., Blake, G. A., & Kessler, J. E. 2002, AJ, 124, 3387

- Itoh, Y., Sugitani, K., Fukuda, N., Nakanishi, K., Ogura, K., Tamura, M., Marui, K., Fujita, K., Oasa, Y., & Fukagawa, M. 2003, ApJ, 586, L141
- Koerner, D. W. & Sargent, A. I. 1995, AJ, 109, 2138
- Kroupa, P. & Bouvier, J. 2003, MNRAS, 346, 369
- Lada, C. J., Depoy, D. L., Merrill, K. M., & Gatley, I. 1991, ApJ, 374, 533
- Lada, C. J. & Lada, E. A. 2003, ARA&A, 41, 57
- Lada, C. J., Muench, A. A., Haisch, K. E., Lada, E. A., Alves, J. F., Tollestrup, E. V., & Willner, S. P. 2000, AJ, 120, 3162
- Lada, E. A., Strom, K. M., & Myers, P. C. 1993, in Protostars and Planets III, ed. E. H. Levy & J. I. Lunine (Tucson: Univ. Arizona Press) 245
- Luhman, K. L. 1999, ApJ, 525, 466
- Luhman, K. L., Rieke, G. H., Lada, C. J., & Lada, E. A. 1998, ApJ, 508, 347
- Luhman, K. L., Rieke, G. H., Young, E. T., Cotera, A. S., Chen, H., Rieke, M. J., Schneider, G., & Thompson, R. I. 2000, ApJ, 540, 1016
- Meyer, M. R. 1996, Ph.D. Thesis
- Miyake, K. & Nakagawa, Y. 1993, Icarus, 106, 20
- Motte, F. & André, P. 2001, A&A, 365, 440
- Motte, F., André, P., & Neri, R. 1998, A&A, 336, 150
- Mundy, L. G., Looney, L. W., & Lada, E. A. 1995, ApJ, 452, L137
- Nuernberger, D., Brandner, W., Yorke, H. W., & Zinnecker, H. 1998, A&A, 330, 549
- Nuernberger, D., Chini, R., & Zinnecker, H. 1997, A&A, 324, 1036
- O'Dell, C. R., Wen, Z., & Hu, X. 1993, ApJ, 410, 696
- O'Dell, C. R. & Wong, K. 1996, AJ, 111, 846
- Osterloh, M. & Beckwith, S. V. W. 1995, ApJ, 439, 288
- Padgett, D. L., Brandner, W., Stapelfeldt, K. R., Strom, S. E., Terebey, S., & Koerner, D. 1999, AJ, 117, 1490

- Pollack, J. B., Hollenbach, D., Beckwith, S., Simonelli, D. P., Roush, T., & Fong, W. 1994, ApJ, 421, 615
- Prosser, C. F., Stauffer, J. R., Hartmann, L., Soderblom, D. R., Jones, B. F., Werner, M. W., & McCaughrean, M. J. 1994, ApJ, 421, 517
- Sault, R. J., Teuben, P. J., & Wright, M. C. H. 1995, in ASP Conf. Ser. 77: Astronomical Data Analysis Software and Systems IV, 433
- Scally, A. & Clarke, C. 2001, MNRAS, 325, 449
- Strom, K. M., Strom, S. E., Edwards, S., Cabrit, S., & Skrutskie, M. F. 1989, AJ, 97, 1451
- Testi, L. & Sargent, A. I. 1998, ApJ, 508, L91
- Warren, W. H. & Hesser, J. E. 1977, ApJS, 34, 207
- Weidenschilling, S. J. 1977, Ap&SS, 51, 153
- Williams, J. P., Andrews, S. M., & Wilner, D. J. 2005, ApJ, 634, 495
- Zapata, L. A., Rodríguez, L. F., Kurtz, S. E., O'Dell, C. R., & Ho, P. T. P. 2004, ApJ, 610, L121

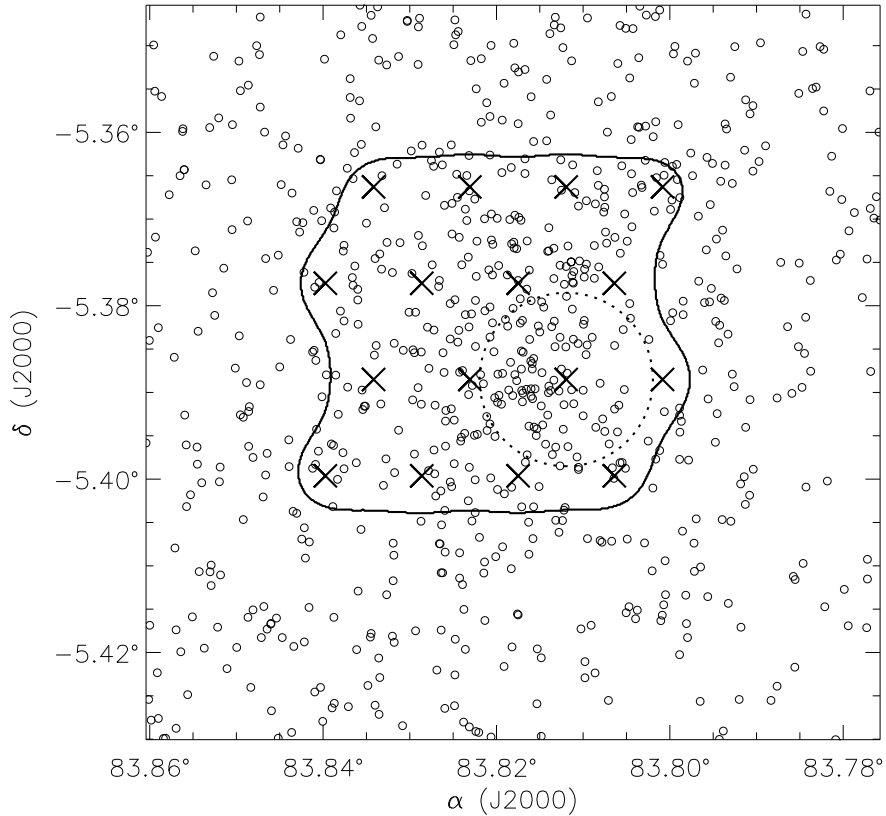


Fig. 1.— Pointing positions for the OVRO mosaic (“X” symbols), plotted over the positions of K -band sources in the ONC (open circles). These K -band source positions are from Hillenbrand & Carpenter (2000), and have been registered to the 2MASS astrometric grid. The unit gain contour of the mosaic (solid curve) and the FWHM of the OVRO primary beam at 100 GHz (dotted circle) are also indicated.

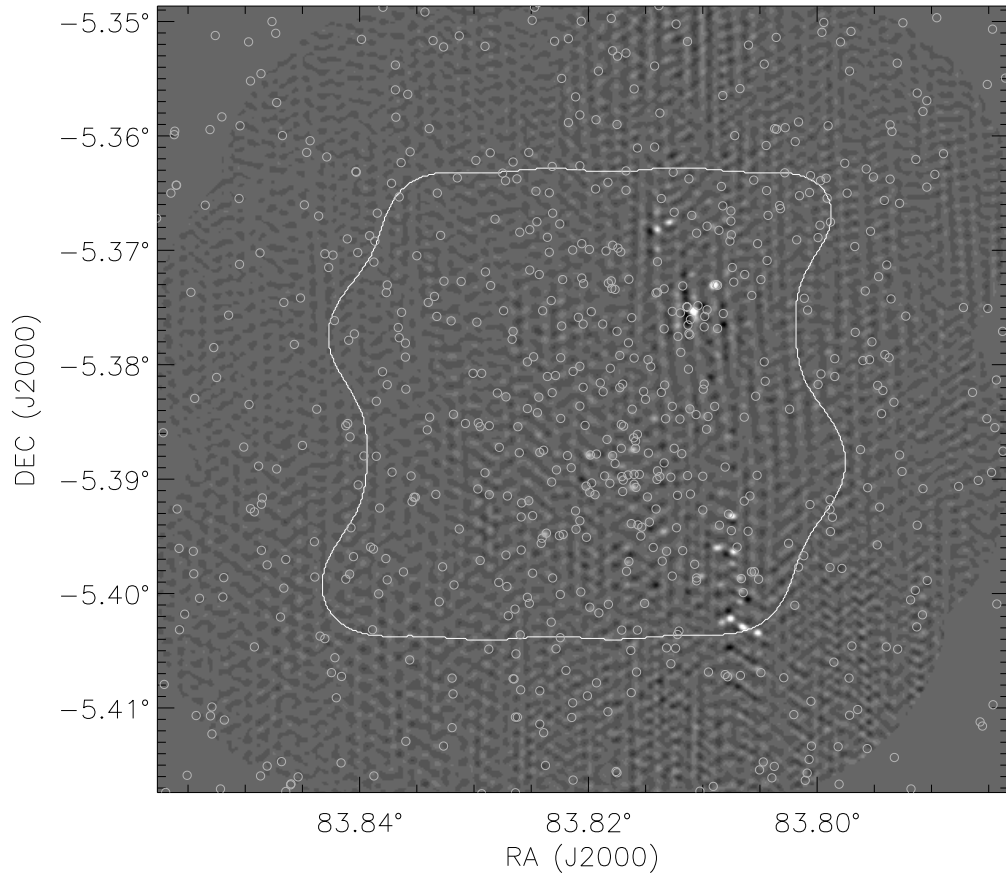


Fig. 2.— The Orion Nebula cluster, imaged in $\lambda 3$ mm continuum with the Owens Valley Millimeter Array (greyscale). Only data observed on long baselines ($r_{uv} > 35$ k λ) were used to create this image, and the FWHM of the synthesized beam is $1.^{\prime\prime}9 \times 1.^{\prime\prime}5$. The unit gain region of the mosaic encompasses a $2.^{\prime\prime}5 \times 2.^{\prime\prime}5$ area, as indicated by the solid contour, and after CLEANing of the bright point sources apparent in this image, the average RMS computed for the residuals within the unit gain contour is ~ 1.75 mJy. Open circles indicate the positions of K -band sources from Hillenbrand & Carpenter (2000).

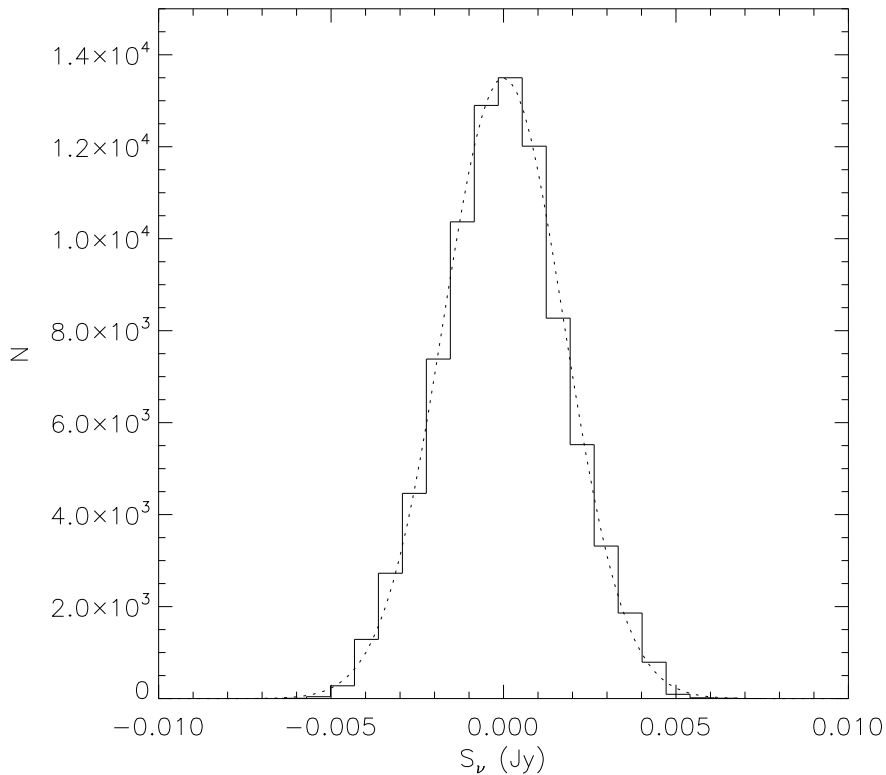


Fig. 3.— Distribution of 3 mm continuum fluxes for all pixels within the unit gain contour of a residual image with bright point sources removed using CLEAN (solid line), and the frequency distribution expected for Gaussian noise with a mean of zero and a standard deviation of 1.75 mJy (dotted line). While the noise varies across the mosaic from 0.88 to 2.34 mJy, as computed in $0'5 \times 0'5$ sub-regions (§2), the average RMS noise is 1.75 mJy.

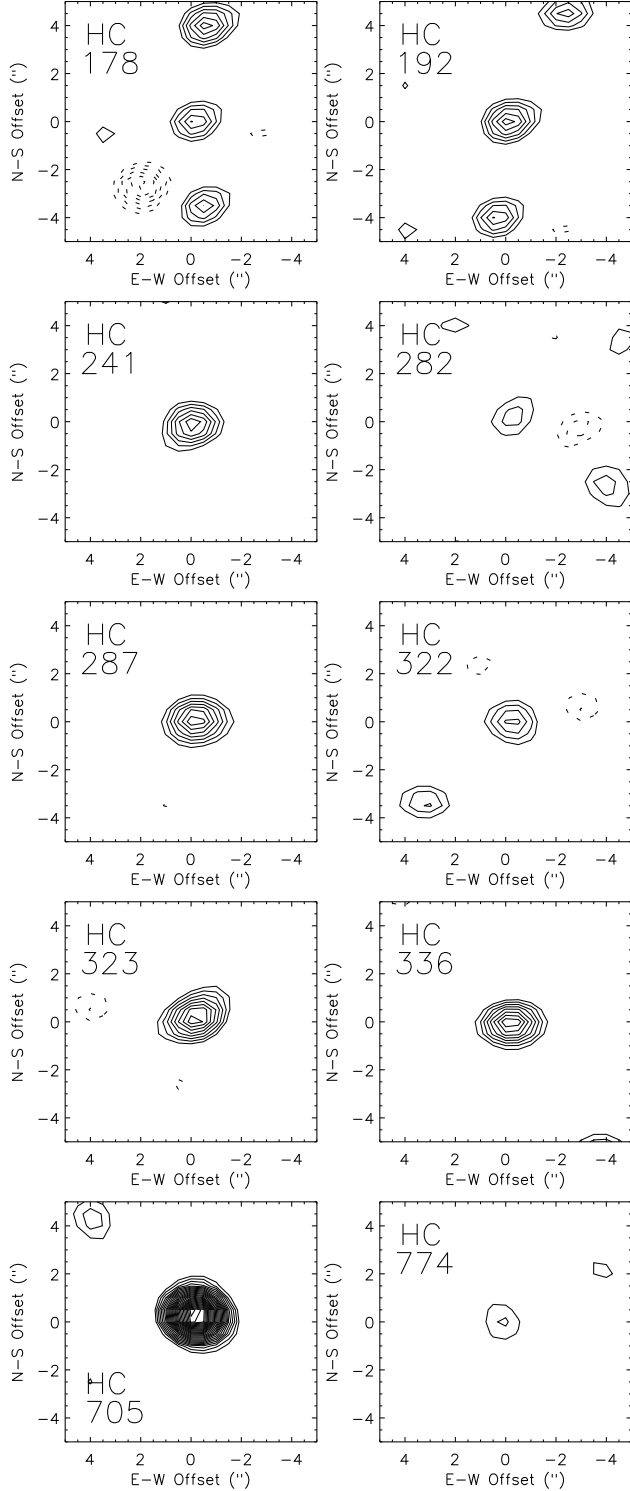


Fig. 4.— Contour images of sources detected at the $\geq 3\sigma$ level in 3 mm continuum emission that correspond to previously known near-IR objects. Contour increments are 1σ , beginning at $\pm 3\sigma$, where σ is determined locally for each object (see §2). Solid contours represent positive emission, and dotted contours trace negative features. HC 705 is the BN object, and HC 336 is $\theta^1\text{OriA}$.

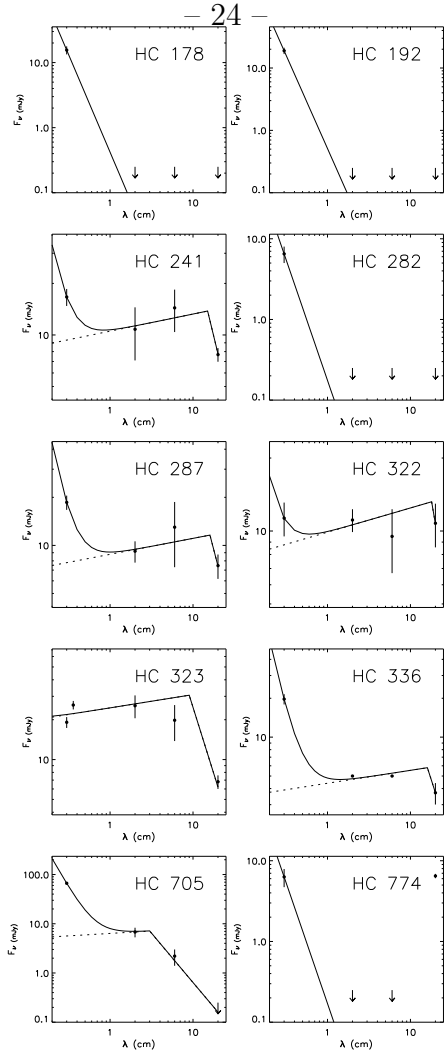


Fig. 5.— Long-wavelength fluxes for our sample (points), along with best-fit models including free-free and thermal dust emission. The free-free emission component is indicated by a dotted line, and the solid-line represents the combined free-free and thermal dust emission. The free-free flux density is proportional to $\nu^{-0.1}$ for optically-thin emission and ν^2 for optically-thick; the emission is thus parameterized by the flux at a single wavelength and a turnover frequency. The emission from cool dust is proportional to $\nu^{2+\beta} \sim \nu^3$ for optically-thin emission with $\beta = 1$. In the case of HC 774, we ignored the 20 cm flux measurement when fitting the model, since we believe this flux probably arises from a different emission mechanism. The 2 and 6 cm emission from HC 336 is highly variable (from $\sim 2 - 80$ mJy; Felli et al. 1993b), and thus the model fit is uncertain for this object.

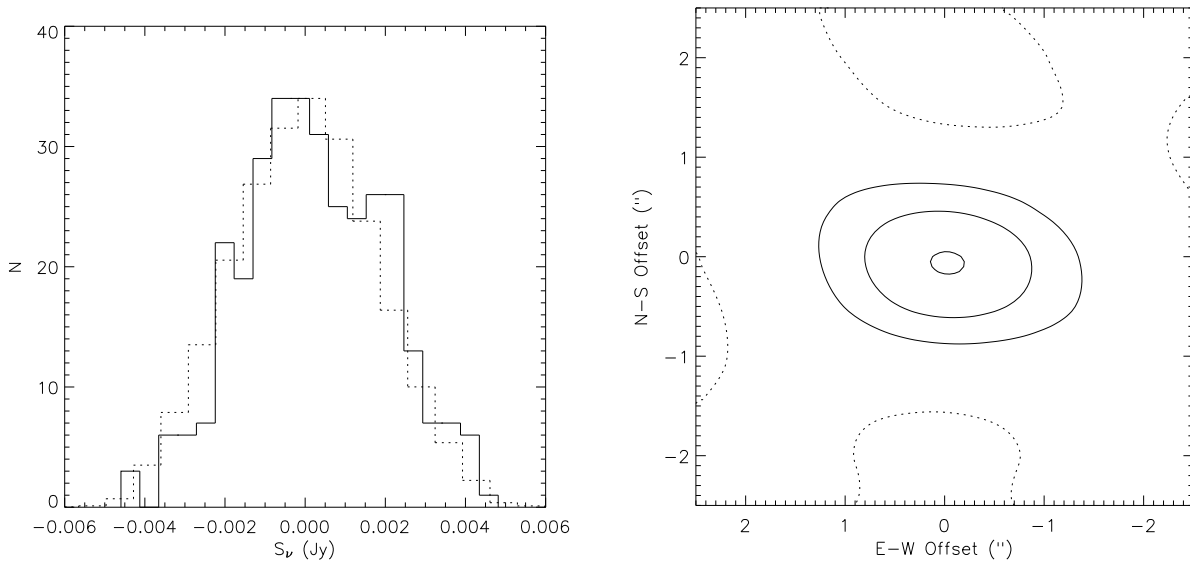


Fig. 6.— (left) Histogram of 3 mm continuum fluxes observed toward positions of 326 near-IR cluster members in the ONC (solid histogram) and the fluxes observed toward the remaining positions within the unit gain contour (dotted histogram). The flux distribution for near-IR sources is biased to positive values with respect to the noise distribution. (right) Average image, obtained by stacking the 3 mm continuum emission observed toward each of the 326 low-mass near-IR sources. Contour levels begin at $\pm 1\sigma$ and the contour interval is 1σ (negative contours are shown as dotted lines). Although none of these 326 objects is detected individually above the 3σ level, average emission is detected for the ensemble at a significance of 3σ , and exhibits a compact morphology centered on the mean stellar position.

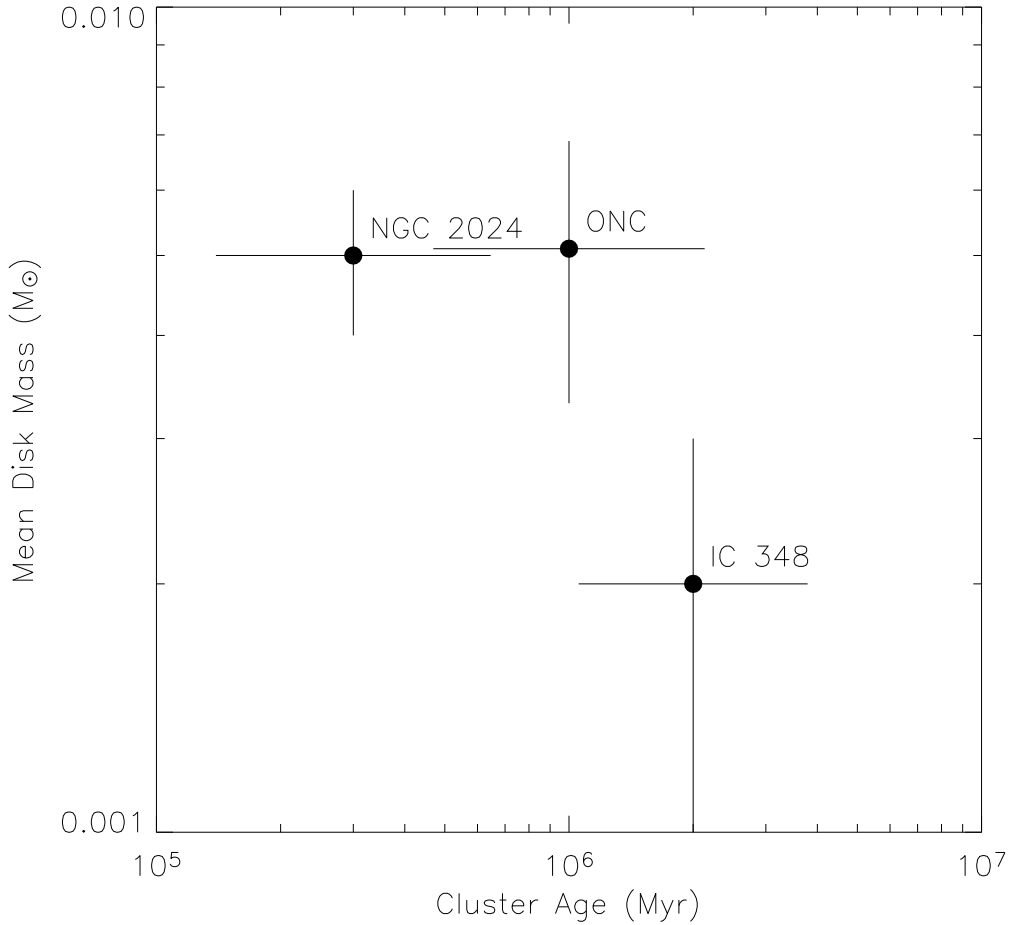


Fig. 7.— Average disk mass as a function of age for the NGC 2024, ONC, and IC 348 clusters. The disk masses are taken from this work, Eisner & Carpenter (2003), and Carpenter (2002), and estimated cluster ages and uncertainties are from Meyer (1996), Ali (1996), Hillenbrand (1997), Luhman et al. (1998), and Luhman (1999).

Table 1. Sources detected in $\lambda 3$ mm continuum with OVRO

ID	α (J2000)	δ (J2000)	S_ν (mJy)	$S_{\nu,\text{dust}}$ (mJy)	$M_{\text{circumstellar}}$ (M_\odot)	Other IDs
OVRO $> 3\sigma$ detections with near-IR counterparts						
HC178*	5:35:13.54	-5:23:59.4	15.55 ± 2.2		0.32 ± 0.05	
HC192*	5:35:13.57	-5:23:55.2	18.92 ± 2.2		0.39 ± 0.05	
HC241	5:35:17.69	-5:23:41.4	16.67 ± 1.9	7.40 ± 5.5	0.15 ± 0.11	OW-177-341,F93-1
HC282	5:35:18.85	-5:23:28.6	6.50 ± 1.5		0.13 ± 0.03	
HC287	5:35:15.82	-5:23:26.6	18.59 ± 1.9	10.80 ± 4.1	0.22 ± 0.09	OW-158-327,F93-13
HC322	5:35:16.30	-5:23:16.6	11.30 ± 1.8	2.50 ± 2.5	0.05 ± 0.05	OW-163-317,F93-7
HC323	5:35:16.74	-5:23:16.6	19.12 ± 1.8	0.00 ± 5.5	0.00 ± 0.10	$\theta^1\text{OriG}$,OW-167-317,F93-6
HC336†	5:35:15.81	-5:23:14.6	19.70 ± 1.8	< 15.80	< 0.33	$\theta^1\text{OriA}$,OW-158-314,F93-12
HC705†	5:35:14.11	-5:22:22.9	66.58 ± 2.1	60.90 ± 4.1	1.26 ± 0.09	BN Object, F93-B
HC774	5:35:18.24	-5:24:13.1	6.31 ± 1.5		0.13 ± 0.03	OW-182-413,F93-O
OVRO $> 5\sigma$ detections without near-IR counterparts						
MM1	05 35 14.12	-05 22 04.6	9.99 ± 1.8		0.21 ± 0.04	
MM2	05 35 14.56	-05 22 19.6	9.67 ± 1.9		0.20 ± 0.04	
MM3*,†	05 35 14.53	-05 22 31.1	70.45 ± 2.0		1.45 ± 0.04	IRc2,F93-I
MM4*	05 35 14.86	-05 22 35.6	14.91 ± 1.9		0.31 ± 0.04	
MM5*	05 35 15.06	-05 22 03.1	26.03 ± 2.0		0.54 ± 0.04	
MM6*	05 35 15.30	-05 22 05.1	26.80 ± 1.9		0.55 ± 0.04	
MM7	05 35 13.72	-05 23 35.6	36.10 ± 2.3		0.74 ± 0.05	
MM8*	05 35 13.69	-05 23 46.6	28.75 ± 1.9		0.59 ± 0.04	
MM9*	05 35 13.72	-05 23 50.6	14.51 ± 2.0		0.30 ± 0.04	
MM10*	05 35 14.03	-05 23 45.6	26.79 ± 2.0		0.55 ± 0.04	
MM11*	05 35 13.56	-05 24 02.6	15.43 ± 2.3		0.32 ± 0.05	
MM12*	05 35 13.49	-05 24 10.6	40.82 ± 2.3		0.84 ± 0.05	
MM13*	05 35 13.76	-05 24 08.1	36.92 ± 2.3		0.76 ± 0.05	
MM14*	05 35 13.92	-05 24 09.1	18.35 ± 1.9		0.38 ± 0.04	
MM15	05 35 13.96	-05 23 57.1	11.72 ± 1.9		0.24 ± 0.04	
MM16	05 35 14.36	-05 23 54.6	16.02 ± 2.0		0.33 ± 0.04	
MM17	05 35 15.16	-05 23 40.6	15.31 ± 2.0		0.32 ± 0.04	
MM18	05 35 15.36	-05 23 05.1	12.52 ± 2.3		0.26 ± 0.05	
MM19*	05 35 15.93	-05 23 45.6	10.31 ± 2.0		0.21 ± 0.04	
MM20*	05 35 15.93	-05 23 50.1	11.94 ± 2.3		0.25 ± 0.05	

Note. — $S_{\nu,\text{dust}}$ is the component of the observed 3 mm emission due to cool dust, determined from a fit to long-wavelength fluxes of a model including thermal free-free emission as well as cool dust emission (see Figure 5). All quoted uncertainties are 1σ , and include only the RMS uncertainties in the measured fluxes; systematic uncertainties associated

with the conversion from flux to mass are not included. *—These objects are located in crowded regions, and thus the observed flux may be contaminated by sidelobe emission from bright, nearby sources. †— θ^1 OriA, BN, and IRc2 are massive stars, and since the dust around these objects may be hotter than the 20 K used to compute $M_{\text{circumstellar}}$, the circumstellar masses are probably overestimated.